Published in final edited form as:
Phys Med Biol. 2012 October 7; 57(19): 6025–6046. doi:10.1088/0031-9155/57/19/6025.

Determination of optical properties in heterogeneous turbid media using a cylindrical diffusing fiber

Andreea Dimofte, **Jarod C. Finlay**, **Xing Liang**, and **Timothy C. Zhu***
Department of Radiation Oncology, University of Pennsylvania, Philadelphia, PA 19104

Abstract

For interstitial photodynamic therapy (PDT), cylindrical diffusing fibers (CDF's) are often used to deliver light. This study examines the feasibility and accuracy of using CDF's to characterize the absorption (μ_a) and reduced scattering (μ_s') coefficients of heterogeneous turbid media. Measurements were performed in tissue-simulating phantoms with μ_a between 0.1 and 1cm^{-1} and μ_s' between 3 and 10 cm^{-1} with CDF's 2 to 4 cm in length. Optical properties were determined by fitting the measured light fluence rate profiles at a fixed distance from the CDF axis using a heterogeneous kernel model in which the cylindrical diffusing fiber is treated as a series of point sources. The resulting optical properties were compared with independent measurement using a point source method. In a homogenous medium, we are able to determine the absorption coefficient μ_a using a value of μ_s' determined *a priori* (uniform fit) or μ_s' obtained by fitting (variable fit) with standard(maximum) deviations of 6% (18%) and 18% (44%), respectively. However, the CDF method is found to be insensitive to variations in μ_s', thus requiring a complementary method such as using a point source for determination of μ_s'. The error for determining μ_a decreases in very heterogeneous turbid media because of the local absorption extremes. The data acquisition time for obtaining the one-dimensional optical properties distribution is less than 8 seconds. This method can result in dramatically improved accuracy of light fluence rate calculation for CDFs for prostate PDT *in vivo* when same model and geometry is used for forward calculations using the extrapolated tissue optical properties.

Keywords

photodynamic therapy; optical properties

1 INTRODUCTION

Photodynamic therapy (PDT) is a treatment modality where light of a given wavelength activates a photosensitizing drug in the presence of oxygen (Dougherty *et al.*, 1998). PDT is often used to treat superficial tumors like those of skin, lung, esophagus and bladder. PDT is approved by the US Food and Drug Administration for the treatment of obstructing lung cancer, micro-invasive lung cancer and obstructing esophageal cancer and Barrett's esophagus with high-grade dysplasia.

Prostate cancer is the most common malignancy in men in the United States (Jemal A, 2011). Several clinical trials of prostate PDT have been published (Weersink *et al.*, 2005a; Weersink *et al.*, 2005b; Nathan *et al.*, 2002; Zaak *et al.*, 2004; Stripp *et al.*, 2004; Verigos *et al.*, 2006; Trachtenberg *et al.*, 2007; Trachtenberg *et al.*, 2008; Patel *et al.*, 2008). Unlike superficial treatments where collimated laser source is used, point sources or cylindrical

*tzhu@mail.med.upenn.edu, Tel 215-662-4043.

diffusing fibers (CDFs) are inserted interstitially into prostate gland using techniques similar to those used in brachytherapy. Our current work focuses on PDT for treatment of solid tumors and lesions in solid organs.

Optical fiber-based isotropic detectors are used in clinical trials of PDT to measure incident and scattered light (Baas *et al.*, 1997; Solonenko *et al.*, 1999; Zhu *et al.*, 2005a). Calculation of the distribution of light in the tissue at points other than the point of measurement, however, requires knowledge of the optical properties of the tissue. Several publications have addressed the issue of determining the optical properties in human (Chen *et al.*, 1997; Essenpreis, 1992; Chen and Hetzel, 1998; Lee *et al.*, 1997; Pantelides *et al.*, 1990; Whitehurst *et al.*, 1994; Lee *et al.*, 1995, 1999; Zhu *et al.*, 2005b; Zhu *et al.*, 2005c) and animal (Arnfield *et al.*, 1993; Chen *et al.*, 1997; Zhu *et al.*, 2003) prostate tissues. Most commonly, the optical properties are determined by measuring the fluence rate at different source-detector separations. By measuring the relative fluence rate for a range of separations, the diffusion approximation of light transport can be used to determine the effective attenuation coefficient μ_{eff} which depends on both μ_a and μ_s'. In an infinite medium, additional information is required to separate the two coefficients. In our previous work, we have separated the optical coefficients using a calibrated measurement of the absolute fluence rate, which also provides information about the *in vivo* fluence rate (Dimofte *et al.*, 2005; Zhu *et al.*, 2005b). These methods are robust and reliable, and rigorously separate the effects of absorption and scattering. However, they suffer one drawback that may make clinical implementation outside of a clinical trial impractical; the optical properties are measured with a different set of sources than those used for treatment, which generally relies on cylindrical diffusive fibers (CDF) (Stripp *et al.*, 2004; D'Amico and Coleman, 1996; Lee *et al.*, 1997; Zhu and Finlay, 2006). This requires insertion of light sources that are not used clinically, which significantly increases the total time required for the procedure.

In this work, we seek to replace the point-like light source used to measure optical properties in our previous work with the CDF's used for treatment light delivery. This new measurement method, while slightly less robust than the point-source method, can be implemented using only the CDF inserted for treatment, and, with proper switching, can be performed during small breaks in treatment that do not significantly extend the treatment time. We anticipate that this will be a significant advance in the effort to bring quantitative light dosimetry to the clinic.

2 METHODS

2.1 Isotropic detectors and cylindrical diffusive fibers (CDF)

The detectors used in this study were optical fiber-based isotropic detectors (Rare Earth Medical, West Yarmouth, MA) of the scattering-tip type (Marijnissen and Star, 1996). The light collected by the detectors was digitized using a photodiode-based in-vivo light dosimetry system (Zhu *et al.*, 2005a). The detectors were calibrated to measure absolute fluence rate in air and corrected for the effects of decreased refractive index mismatch in the liquid and solid phantoms (Star *et al.*, 1988; Star, 1997). In the case of our liquid phantoms, the reading was increased by a factor of 1.8 (Zhu *et al.*, 2005a). Each corrected profile was divided by the source power.

To account for the effect of the non-uniform source strength distribution of the CDF's, the light distribution was measured in air using an isotropic detector scanned along each CDF. Figure 1 shows a typical in-air light fluence distributions of CDF's of different lengths (2, 3 and 4 cm).

2.2 Phantom preparation

Optical properties were measured in liquid and solid phantoms. The liquid tissue simulating phantoms were made of separate scattering and absorbing components, namely fat emulsion (Liposyn III, 30% Abbott Lab, North Chicago, IL) and India ink (Higgins black India ink #4418, Higgins, Bellwood IL). The phantoms were placed in a plastic container that was painted in black and was large enough ($18.2 \times 14.6 \times 7.7$ cm^3) to avoid scattering from the boundaries. This type of phantom has been described in the literature by Madsen (Madsen, 1992).

RTV silicon phantoms were prepared using the method described by Bays *et al* (Bays *et al.*, 1997) and Beck *et al* (Beck *et al.*, 1998). These phantoms are composed of a base compound (RTV12A), curing agent (RTV12C), absorber (Carbon black) and scatterer (titanium dioxide (TiO_2)). The inhomogeneous solid phantom used for our measurements was composed of a uniform phantom with $\mu_a = 0.2$ cm^{-1} and $\mu_s' = 13 cm^{-1}$ and three small in homogeneities, each having the same scattering coefficient of 13 cm^{-1}, and absorption coefficients of 0.1, 0.5 and 0.9 cm^{-1}.

2.3 Independent Characterization of phantom optical properties

The optical properties were calculated based on the concentrations of the India ink and intralipid (or carbon black and TiO_2 in the solid phantoms), and independently determined in liquid phantoms using measurements based on a point source in the liquid phantoms (Dimofte *et al.*, 2005). The experimental setup for point source measurement is shown in Figure 2. We used a device consisting of 2 parallel catheters separated by 0.5 cm. An isotropic point source was placed in one of the catheters and connected to a 730 nm diode laser (Diomed 730, Cambridge, UK). An isotropic detector was placed in the other catheter. The isotropic detector was connected to a light dosimetry system and its position was controlled by a translation stage, allowing the detector to be scanned along its catheter parallel to the light source. Fluence rate measurements were made at 0.05 mm intervals along its movement. The data acquisition speed for a scan of 10 cm distance with 2000 data points was about 8 seconds, giving a scan speed of 12.5 mm/s.

2.4 Interstitial phantom measurements

Cylindrical diffusing fibers (CDF's) with active lengths of 2 to 4 cm were used as light sources and were placed inside the phantom through transparent plastic catheters (Flexi-needle, Best medical International, Springfield, VA). A 15-W, 732 nm diode laser (Model 730, Diomed, Ltd., Cambridge, United Kingdom) was used as the light source. The catheters were aligned to the prostate using a template that provided spacing of 0.5cm in lateral and vertical directions (Fig. 2a). The fluence rate was measured using a 0.5 mm scattering tip isotropic detector that was moved along a parallel catheter using a motorized probe described above. Measurements were taken in both a solid prostate-simulating phantom and liquid phantoms, as shown schematically in Fig. 2a and Fig. 2b, respectively.

Transparent catheters were inserted in parallel, through a template, into the prostate with the guidance of a transrectal ultrasound (TRUS) unit. The CDFs were placed in the catheters, in such way that it would cover the entire prostate, as shown in Fig. 3(b). The placement in the prostate phantom of each of the twelve CDF's (S1 through 12) as well as the placement of the six detectors (D1 through D6) is shown in Fig. 3(a). For the point source measurements, the position of the light sources and detectors were switched, i.e., point sources are now placed in positions labeled D1 – D6 while 12 isotropic detectors were placed in positions labeled S1 – S12. There are cases when the catheter exits the prostate phantom and CDFs are actually placed partially in the exterior of the phantom. This will produce a scan that started in the air for the initial part of the scan, and then is continued in the phantom. When

analyzing this data set, we fit the entire range, but we ignore the optical properties obtained in the phantom's exterior.

As in a clinical prostate PDT procedure, even though the tips of all catheters were planned to be aligned on the same apex plane, they deviated to up to 1 cm. All measured profiles were therfore shifted to align the calculated light fluence rate with the measured light fluence rate so that the starting point of the CDF is defined as starting point, i.e., 0 cm.

2.5 Data analysis and source modeling

To rigorously determine the optical properties in a heterogeneous phantom, one has to solve the inverse problem for the steady state light diffusion equation, which has the form:

$$\mu_a \Phi - \nabla \cdot (D \nabla \Phi) = S, \tag{1}$$

where $D=1/3\mu_s'$ is the diffusion coefficient. Both optical properties (μ_a and μ_s') are assumed to be spatially variant.

In our previous work using point-like sources to determine optical properties interstitially, we have used the diffusion approximation to the optical radiative transport equation an in infinite homogeneous medium,

$$\Phi = S \frac{3\mu_s'}{4\pi r} e^{-\mu_{eff} r}, \tag{2}$$

where r is the distance from the source and S is the source power. Given an calibrated measurement of fluence rate in the tissue, this model can rigorously separate μ_a and μ_s' using standard nonlinear minimization techniques (Dimofte *et al.*, 2005).

When this model is extended to a CDF of finite length, the model and the fitting become more complicated. We model a CDF as a sum of N point sources. In an infinite, homogeneous medium, the corresponding expression for the fluence rate is:

$$\Phi = \sum_{i=1}^{N} s_i \frac{3\mu_s'}{4\pi r_i} e^{-\mu_{eff} r_i} \tag{3}$$

Where r_i is the distance from the i^{th} point source to the point of interest, and s_i is the power of the i^{th} point source (see Fig. 4). The values of s_i are determined by measurements of the distribution of light emitted along the length of the CDF (Φ_{air}) as described above (see Fig. 1) and the total source power of the CDF (S_{meas}), and calculated subject to the constraints:

$$S_{meas} = \sum_{i=1}^{N} s_i, \text{ and} \tag{4a}$$

$$\frac{s_i}{S_{meas}} = \frac{\Phi_{air} \cdot \Delta x}{\int \Phi_{air}\, dx}, \tag{4b}$$

where Δx is the spacing between the point sources used to model the CDF. In the parallel-catheter geometry employed here, we rely on the falloff with distance along the catheter to separate μ_a and μ_s'. For a point source, this problem is well-posed, as we have demonstrated previously (Dimofte *et al.*, 2005). In the limit of an infinitely long CDF, the problem

becomes ill posed because of the symmetry of the source; in the parallel-catheter geometry, we vary the position of the detector along a line parallel to the source axis, so an infinite source yields no falloff information. In reality, we have the intermediate situation of a finite but extended source. We take advantage of this by collecting data beyond the end of the source, including the falloff of light beyond the source. Accounting for heterogeneities in addition to the extended source poses a solvable but computationally challenging problem. To address this, we have implemented a two-step fitting algorithm.

First, the entire curve is fit assuming homogeneous optical properties using the Nelder-Mead nonlinear multidimensional minimization algorithm available in Matlab (fminsearch). This step takes into account the measured variations in the intensity of the CDF, but not variations in optical properties. A third free parameter is the alignment of the source and detector along the *z* (longitudinal) direction. The result is a three-dimensional optimization that converges rapidly, ensures proper alignment of the source and detector positions, and produces uniform optical properties.

In reality, the optical properties of tissue are rarely truly uniform. The second step in the fitting algorithm is designed to account for variations in optical properties. We have previously demonstrated the ability of similar measurements using point sources of illumination to constrain both μ_a and μ_s' (Dimofte *et al.*, 2005). In the case of CDFs, however, the number of free parameters (one value of μ_a and one value of μ_s' for each spatial location) becomes large compared to the number of measurements used to constrain them. While there are up to 1000 points per scan, they are made in close physical proximity with a single illumination source, so they do not constitute independent measurements. Therefore, it is impractical to determine μ_a and μ_s' at every location. Instead, we assume that μ_s' is uniform within each scan, and calculate the variation in μ_a. To investigate the influence of uncertainty in μ_s' determination, we have also performed fits using a modified version of this first step, in which the value of μ_s' is fixed and the free parameters are μ_a and the source alignment in the *z* direction. This required *a priori* knowledge of μ_s', so it is necessary to use independent methods, such as point source measurements, to determine μ_s'.

The scan is divided into regions determined by the resolution of the desired optical property map. The medium is assumed to consist of optically homogeneous slabs whose borders are perpendicular to the CDF's long axis, as shown in Fig. 4. The (chi-squared) deviation between the initial (uniform optical properties) fit and the measured data within each region is calculated. Because this step allows μ_a to vary spatially, we must take into account the fact that the space between the source and the point of interest may include regions with different μ_a. We replace equation 4 with

$$\Phi = \sum_{i=1}^{N} s_i \frac{3\mu_s'}{4\pi r_i} e^{-\bar{\mu}_{eff}\, r_i}, \tag{5}$$

where the mean effective attenuation coefficient is the average weighted by the fraction of the line connecting the source and the point of interest that falls within each bin:

$$\bar{\mu}_{eff} = \frac{1}{r_i} \sum_{j=1}^{n_{bin}} r_{ij}\, \mu_{eff\,(ij)}, \tag{6}$$

Here, n_{bin} is the number of optical properties bins between the source and detector, $\mu_{eff(ij)}$ is the effective attenuation coefficient of the j^{th} bin, and r_{ij} is the distance along the line

connecting the source and detector that falls within the j^{th} bin, as shown in Fig. 4. Hence, each term in the sum in Eq. 4 requires a separate weighted average to calculate μ_{eff}.

Each region's μ_a is fit individually. The fit uses as its penalty function the chi-squared goodness-of-fit statistic calculated over the region being optimized and the adjacent four regions (two on either side), χ_n^2.

$$\chi_n^2 = \sum_k \left(\frac{\Phi_{calc}(k) - \Phi_{meas}(k)}{\sigma_{meas}(k)} \right)^2, \quad (7)$$

Where $\Phi_{meas}(k)$ and $\sigma_{meas}(k)$ are the measured fluence rate and estimated measurement uncertainty at the k^{th} measurement point, respectively, and $\Phi_{calc}(k)$ is the fluence rate calculated for the k^{th} measurement point using equation 5. The sum in equation 7 includes all measurement points within regions $n-2$ to $n+2$. This ensures that the optimal μ_a will be consistent with the continuous measured data. At each iteration, the value of χ_n^2 is calculated for each region. The regions are ranked and fit in order of decreasing χ_n^2. A simple, one-dimensional, nonlinear fit (fminbnd, Matlab) is performed to optimize only the value of μ_a within the selected region. In each iteration, the value of μ_a in each region is constrained to change by no more than 30% in either direction, to prevent spatial oscillations in the solution. The value of 30% was chosen empirically as a reasonable balance between conversion speed and solution smoothness. The cycle of fitting is repeated until subsequent fits decrease the maximum value of χ_n^2 by less than 5%. A flowchart of this fitting process is shown in Fig. 5.

To evaluate the sensitivity of our model and algorithm to μ_a and μ_s', we generated an ideal fluence profile Φ_0 (z) using Eq. 2 assuming homogenous optical properties μ_{a0} and μ_{s0}'. We then varied μ_a and μ_s' across a wide range and calculated the Root-Mean-Square (RMS) deviation between the resulting Φ profile and Φ_0 (z). The resulting deviation surface is analogous to χ^2, but does not take into account the uncertainty in the measurement. It therefore describes the inherent sensitivity of the model to variations in optical properties.

The form of Eq. 5 is similar to that referred to as "model 1" in our previous work on light fluence rate calculations in heterogeneous media (Li and Zhu, 2008). This formalism has been shown to agree with measurements in heterogeneous media to within 35% (Li and Zhu, 2008). Although the formula can be improved to achieve better agreement with measurements, it comes with added computational burden and is thus not used in the current study. We compared the results of our current model (Eq. 5) with those of a finite element method (FEM) calculation using the diffusion equation (equation 1).

3. RESULTS

Measurements of the optical properties of a homogeneous sample were within clinically acceptable uncertainties, as shown in table 1. When the value of μ_s' was allowed to vary (columns labeled 'uniform source variable - μ_s' fit'), the optical properties were determined with slightly larger uncertainty than when the value of μ_s' is fixed based on *a priori* knowledge (columns labeled 'uniform source fixed – μ_s fit'). CDF methods are insensitive to the value of μ_s', a point illustrated graphically in Fig. 6(b). While the overall trend in best-fit μ_s' values follows the true values, individual points deviate by more than a factor of 2 (Fig. 6b). The results in homogeneous phantoms illustrate that the absorption coefficients obtained using CDF are quite reliable, independent of the value of corresponding μ_s'.

To evaluate the effect of approximating the physical source distribution with a uniform distribution, we fit a subset of the data shown in table 1 with both the measured source distribution (as shown in Fig. 1) and the uniform approximation. The results are summarized in Table 2. Changing the source distribution can influence the shape of the best-fit absorption distribution. This phenomenon is illustrated in Fig. 7(a & b), which shows the best fit of absorption coefficient based on the in air source profile (Fig. 7a) and the uniform profile (Fig. 7b) based on the variable-μ_s' method for a selected homogeneous phantom. Data are shown for 2, 3 and 4 cm long CDF's. The solid lines represent the expected value of μ_a. The uniform source strength gives more accurate recovery of μ_a. It is possible that the in-air scan may not completely represent the intensity profile distribution in all directions and that a uniform distribution may result in a better overall description of the intensity profile.

Figure 8(a) through (h) show the fluence rate per unit source strength (upper graph, left vertical axis), the source strength (upper graph, right vertical axis), and absorption coefficients vs. position along CDF (lower graph) obtained from various detector - CDF pairs in the solid prostate phantom for a 4-cm long CDF. Figure 8(a) is for light fluence rate per source strength and source strength distribution for the pair detector 1 and source 1 (D1–S1). The dots represent the data, the red line represents the fit, and the solid and dotted blue lines show the source strength for uniform and actual distributions of that particular CDF based on the in-air scan (Eq. 4), respectively. Notice the origin of x-axis (0) is always aligned with the starting edge of the CDF. Figure 8(b) plots the absorption coefficient vs. distance as determined along the CDF direction. Figure 8(c) and d show the results for the detector 2 and source 3 (for a 4cm long CDF). In Fig. 8(e) and (f), the results are shown for detector 3 and source 4 (4 cm long CDF). Figures 8(g) and (h) plot the results for detector 5 and source 11. The summary results comparing the measured and the known optical properties are listed in Table 3.

The inherent sensitivity of our model to the absorption and scattering parameters is illustrated in Fig. 9. The contours represent lines of iso-RMS deviation between an ideal fluence distribution calculated with optical properties μ_a and μ_s', and one calculated with the nominal optical properties μ_{a0} and μ_{s0}', 0.5 and 7 cm-1, respectively in this example. The narrow, nearly horizontal contours indicate that the algorithm is inherently more sensitive to μ_a than μ_s'.

4. DISCUSSION

The uncertainties of extrapolating the absorption coefficients μ_a using CDF in homogeneous phantoms are examined in detail in Table 1 and Fig. 6a. The standard (maximum) deviation for determining μ_a in homogeneous optical phantom is 6% (18%) and 18% (44%) for uniform source fixed-μ_s' fit and uniform source variable-μ_s' fit, respectively (Table 1). The uniform source fixed-μ_s' fit uses a uniform source strength along CDF and use the prior known μ_s' while the uniform source variable-μ_s' fit uses a uniform source strength along CDF and allow the software to determine μ_s' on its own, which can be up to 84% different from the true μ_s'. Figure 6a shows the same results in Table 1 graphically. To further examine the impact of errors of μ_s' on the determination of μ_a, we have also shown the extrapolated μ_a data in Table 1 when μ_s' is deliberately set to ±20% from its true values. In this case, the standard (maximum) deviation for determining μ_a in homogeneous optical phantom is 15% (46%).

The uncertainty of extrapolating the reduced scattering coefficients μ_s' in a homogeneous phantom is shown in Table 1 and Fig. 6b for different lengths of CDF. The sensitivity for determination of μ_s' is quite poor using CDFs. This results from the fact that the

independent determination of μ_a and μ_s' requires two independent measurements. In the case of the point source, these are the absolute value of the fluence rate and the rate of falloff with distance. It is only beyond the ends of a finite CDF that the differentiation between μ_a and μ_s' approaches the point-source situation. As a result, independent method such as the point source method should be used to determine μ_s'.

The idealized case of synthetic data produced with homogeneous optical properties provides insight into the sensitivity of the fitting algorithm, as shown in Fig. 9, which plots contours of relative RMS deviation in signal measured from a 4-cm CDF in a homogenous medium. The deviation about the true μ_a and μ_s' (0.5 and 7 cm^{-1}, respectively) changes rapidly with μ_a but only slowly with μ_s'. In fact, the 1% RMS error contour encompassed μ_s' values from 5 to 10 cm^{-1}, but μ_a values only from 0.48 to 0.51 cm^{-1}. Similar results are found across the range of optical properties measured in this work (data not shown). When fitting real data, this deviation is essentially the chi-squared used to constrain the fit. It is therefore not surprising that finding the minimum chi squared constrains μ_a relatively tightly, but μ_s' only very loosely. The best fit optical properties lie in a long, narrow "valley" in χ^2 space, aligned nearly parallel to the μ_s' axis, making the best fit value of μ_s' very sensitive to any noise in the measurement.

Figure 7 shows that when we apply the heterogeneous algorithm using CDF to a homogenous phantom, the code is able to recover the absorption coefficient μ_a correctly, even though one does not assume that μ_a were homogeneous. As a result, the data in Table 1, is an average of data obtained in 9 phantoms, each is similar to Fig. 7(b). Figure 7(b) represents the uncertainties one would expect using uniform source strength.

Similar values of μ_a are also obtained whether one uses the realistic source strength distribution for the CDF (using the in-air scan) or assuming the CDF has uniform source strength distribution, see Fig. 7. A summary of accuracy in determining absorption coefficient using CDF methods with uniform source strength distribution (uniform fit) and actual source strength distribution (in-air scan fit) in liquid phantom is shown in Table 2. The percentage difference between extrapolated mean and the true μ_a is up to 7% for the uniform source strength and up to 12% for the in-air source strength profile. The standard deviation of μ_a for each μ_a condition is also about the same (see Table 2). However, the spatial distribution of μ_a deviates generally more from the true μ_a for the in-air source strength profile than that for the uniform source strength profile. The reason is unknown but we speculate that the actual in-air source strength may have a directional dependence which is not accounted for in the current study.

The comparison between μ_a obtained using point sources and CDF methods shows good agreement in heterogeneous prostate phantom (Fig. 8). This is indicative that our approximation (Eq. 5) used in calculating light fluence rate in heterogeneous medium yields acceptable accuracy. Using CDF method to extrapolate μ_a is more sensitive in showing heterogeneity than using the point source method simply because the step size for moving the point source is kept at 0.5 cm which can result in missing the regions with large heterogeneity. Comparison of the fit μ_a also agreed with the expected absorption coefficients as shown in Fig. 3(a). For D1–S1 combination (Fig. 8b), the fit μ_a (0.6 – 1.0 cm^{-1}) is in the region of the expected μ_a (0.9 cm^{-1}) for heterogeneity 3. For D2–S3 combination (Fig. 8d), the fit μ_a (0.15 – 0.2 cm^{-1}) is in good agreement with the expected μ_a (0.2 cm^{-1}) for the background. For D3 – S4 combination (Fig. 8f), the fit μ_a (0.2 – 0.43 cm^{-1}) is in between the μ_a for the background (0.2 cm^{-1}) and the μ_a (0.5 cm^{-1}) for heterogeneity 1. For D5 – S11 combination (Fig. 8h), the fit μ_a (0.1 – 0.15 cm^{-1}) is in between the μ_a for the background (0.2 cm^{-1}) and the μ_a (0.1 cm^{-1}) for heterogeneity 2.

Table 3 summarizes the percentage difference between the true values and the extrapolated values.

We concluded from the uncertainty analysis of the results in Fig. 8 and Table 3 that one can accurately extrapolate μ_a to an standard(maximum) deviations of 30% (69%) using the uniform source strength and 27% (57%) using the in-air profile. Substantial differences between measured and expected values of the phantom could be attributed to many errors: first, there is the possibility of a breakdown of our algorithm in a heterogeneous medium. However, we have shown with forward FEM calculation in the heterogeneous phantom (Fig. 8) that the error caused by our algorithm is not significant, resulting in an error of up to 30% in light fluence rate given a very heterogeneous condition. The second significant source of error is due to the physical locations of the distances between CDFs (or point sources) and detectors. In the algorithm, they were assumed to be exactly on the 0.5cm grid. In reality, they are most likely not, very possible up to 3mm off from the grid. This is probably the main source of error. The important point is that we can use the extrapolated optical properties and predict the light fluence correctly. It is impossible to detect nonparallel or curved catheter placement from the data alone except in the most extreme cases. Therefore, an independent measurement of catheter position is required to address this uncertainty. Work is ongoing to make use of real-time or near-real-time ultrasound imaging to determine the position, angle, and curvature of the catheters placed in the prostate. Once these positions are determined, they can be incorporated into the algorithm described here with only trivial modification.

In Fig. 10, fitting results from detector 5 and S11 are compared with optical properties reconstructed by solving the inverse problem of the diffusion equation directly using CDF (Wang and Zhu, 2009) based on the finite element method (FEM) to solve Eq. 1. A modified version of the NIRFAST user code (Dehghani *et al.*, 2008) was used to perform the reconstruction, in which forward calculations were performed to generate light fluence rate and Jacobian matrices were calculated to iteratively find the reconstructed optical properties. In this reconstruction, light fluence measurement results for all detectors adjacent to the CDFs are used (see Fig. 3a), and 2355 node points were modeled to generate the mesh. For each CDF, 21 data points were used for each detector, and a total number of 72 source-detector pairs were used in the reconstruction. As seen in Fig. 10(b), the FEM-reconstructed optical properties are plotted from 21 points in the region between detector 5 and S11, so that they can be compared with the fitting results, which also represent the optical properties in the whole region between the S11 and detector 5. In this region, there are at least 1×1×15 unknown nodes used in the reconstruction. As seen in Fig. 10(a), the FEM-reconstructed μ_a values have similar trend (represented by their mean values and standard deviations) along the z direction. However, in the FEM reconstruction method, the μ_s' is not constrained to be homogeneous, which may cause some differences compared to the fitting results. The agreement in μ_a between that using CDF method vs. directly solving the inverse FEM gives us confidence in the proposed method to determine the tissue optical properties using CDF intended for interstitial treatment.

One of the major advantage of using the CDF intended for prostate PDT treatment directly to extrapolate optical properties is that the clinically relevant light fluence rate distribution in each detector channel is used to determine the optical properties. This fluence rate distribution can therefore be exactly reproduced, even if there are errors in positioning of the CDF, nonuniform source strength distributions of CDF, or approximations made in the computational model, as long as the forward calculation geometry and computational model are the same as those used to determine optical properties. Figure 11 shows excellent agreement between the measured and calculated light fluence rate profile for each detector location (D1 – D6) during PDT treatment. As a result, we expect a dramatic improvement in

the accuracy of the forward calculation of the light fluence rate distribution during PDT, making it possible to reducing the errors of light fluence rate calculation to within ±5% in a heterogeneous prostate gland.

5. CONCLUSIONS

We showed that it is possible to accurately determine the absorption coefficient in homogeneous turbid media using CDFs with standard(maximum) deviations of 7% (23%) assuming uniform source strength distribution. This accuracy is not remarkable by the standards of optical dosimetry or optical tissue diagnosis. Nonetheless, it represents a significant advance for the particular case where interstitial optical property measurement is used as part of the dosimetry calculation for light-based therapy such as PDT. In these cases, the ability to determine optical properties and detect optical inhomogeneities using the sources used for treatment light delivery has several distinct advantages. First, the fact that the treatment delivery sources are used for optical property determination ensures that any calculations of treatment fluence rate based on these optical properties will be correct, at least in the region where the measurements were made, as this is the definition of a good fit. The result is that the uncertainty in the calculations based on these optical properties may actually be lower than the uncertainties in the optical properties themselves. Second, these measurements can be made immediately before the onset of treatment irradiation, without the need to reposition or replace optical fibers, and can easily be repeated during the treatment as a means of monitoring treatment-induced optical property changes. This reduces concern about differences in positioning between measurement and treatment, and reduces the time that optical property characterization adds to treatment. Finally, the use of a single set of sources and detectors for optical characterization, dosimetry, and treatment will allow the development of integrated, computer-controlled systems for PDT delivery. This is an important direction in the future development of clinical PDT, and has been an ongoing effort in our laboratory (Zhu and Finlay, 2006).

Acknowledgments

Work supported by NIH grants R01 CA109456 and P01 CA87971.

References

Arnfield MR, Chapman JD, Tulip J, Fenning MC, McPhee MS. Optical properties of experimental prostate tumors in vivo. Photochem Photobiol. 1993; 57:306–11. [PubMed: 8451295]

Baas P, Murrer L, Zoetmulder FAN. Photodynamic therapy as adjuvant therapy in surgically treated pleural malignancies. Br J Cancer. 1997; 76:819–26. [PubMed: 9310252]

Bays R, Wagnieres G, Robert D, Theumann JF, Vitkin A, Savary JF, Monnier P, van den Bergh H. Three-dimensional optical phantom and its application in photodynamic therapy. Lasers Surg Med. 1997; 21:227–34. [PubMed: 9291079]

Beck GC, Akgün N, Rück A, Steiner R. Design and characterisation of a tissue phantom system for optical diagnostics. Laser Med Sci. 1998; 13:160–71.

Chen Q, Hetzel FW. Laser dosimetry studies in the prostate. J Clin Laser Med Surg. 1998; 16:9–12. [PubMed: 9728124]

Chen Q, Wilson BC, Shetty SD, Patterson MS, Cerny JC, Hetzel FW. Changes in in vivo optical properties and light distributions in normal canine prostate during photodynamic therapy. Radiat Res. 1997; 147:86–91. [PubMed: 8989374]

D'Amico AV, Coleman CN. Role of interstitial radiotherapy in the management of clinically organ-confined prostate cancer: the jury is still out. J Clin Oncol. 1996; 14:304–15. [PubMed: 8558212]

Dehghani H, Eames ME, Yalavarthy PK, Davis SC, Srinivasan S, Carpenter CM, Pogue BW, Paulsen KD. Near infrared optical tomography using NIRFAST: Algorithm for numerical model and image reconstruction. Commun Numer Meth Eng. 2008; 25:711–32.

Dimofte A, Finlay JC, Zhu TC. A method for determination of the absorption and scattering properties interstitially in turbid media. Phys Med Biol. 2005; 50:2291–311. [PubMed: 15876668]

Dougherty TJ, Gomer CJ, Henderson BW, Jori G, Kessel D, Korbelik M, Moan J, Peng Q. Photodynamic Therapy. J Natl Cancer Inst. 1998; 90:889–905. [PubMed: 9637138]

Essenpreis, M. PhD Thesis. London: University College London; 1992. Thermally induced changes in optical properties of biological tissues.

Jemal ABF, Center MM, Ferlay J, Ward E, Forman D. Global cancer statistics. CA Cancer J Clin. 2011; 61:69–90. [PubMed: 21296855]

Lee LK, Whitehurst C, Chen Q, Pantelides ML, Hetzel FW, Moore JV. Interstitial photodynamic therapy in the canine prostate. Br J Urol. 1997; 80:898–902. [PubMed: 9439405]

Lee LK, Whitehurst C, Pantelides ML, Moore JV. In situ comparison of 665 nm and 633 nm wavelength light penetration in the human prostate gland. Photochem Photobiol. 1995; 62:882–6. [PubMed: 8570727]

Lee LK, Whitehurst C, Pantelides ML, Moore JV. An interstitial light assembly for photodynamic therapy in prostatic carcinoma. BJU Int. 1999; 84:821–6. [PubMed: 10532979]

Li J, Zhu TC. Determination of in vivo light fluence distribution in a heterogeneous prostate during photodynamic therapy. Phys Med Biol. 2008; 53:2103–14. [PubMed: 18369279]

Madsen S. The use of India ink as an optical absorber in tissue-simulating phantoms. Phys Med Biol. 1992; 37:985–93. [PubMed: 1589459]

Marijnissen JP, Star WM. Calibration of isotropic light dosimetry probes based on scattering bulbs in clear media. Phys Med Biol. 1996; 41:1191–208. [PubMed: 8822784]

Nathan TR, Whitelaw DE, Chang SC, Lees WR, Ripley PM, Payne H, Jones L, Parkinson MC, Emberon M, Gillams AR, Mundy AR, Bown SG. Photodynamic therapy for prpstate cancer recurrence after radiotherapy: A phase I study. J Urol. 2002; 168:1427–32. [PubMed: 12352410]

Pantelides ML, Whitehurst C, Moore JV, King TA, Blacklock NJ. Photodynamic therapy for localised prostatic cancer: light penetration in the human prostate gland. J Urol. 1990; 143:398–401. [PubMed: 2299739]

Patel H, Mick R, Finlay J, Zhu TC, Rickter E, Cengel KA, Malkowicz SB, Hahn SM, Busch TM. Motexafin lutetium-photodynamic therapy of prostate cancer: short- and long-term effects on prostate-specific antigen. Clin Cancer Res. 2008; 14:4869–76. [PubMed: 18676760]

Solonenko M, Zhu TC, Vulcan T. Commissioning of the isotropic light dosimetry system for photodynamic therapy. Med Phys. 1999; 26:1124.

Star WM. Light dosimetry in vivo. Phys Med Biol. 1997; 42:763–87. [PubMed: 9172258]

Star WM, Marijnissen JP, Avan Gemert MJC. Light dosimetry in optical phantoms and in tissues: I. Multiple flux and transport theory. Phys Med Biol. 1988; 33:437–54. [PubMed: 3380885]

Stripp D, Mick R, Zhu TC, Whittington R, Smith D, Dimofte A, Finlay JC, Miles J, Busch T, Shin DAK, Tochner Z, Malkowicz SB, Glatstein E, Hahn SM. Phase I trial of motexafin-lutetium-mediated interstitial photodynamic therapy in patients with locally reccurent prostate cancer. Proc SPIE. 2004; 5315:88–99.

Trachtenberg J, Bogaards A, Weersink RA, Haider MA, Evans A, McCluskey SA, Scherz A, Gertner MR, Yue C, Appu S, Aprikian A, Savard J, Wilson BC, Elhilali M. Vascular targetd photodynamic therapy with palladium-bacteriopheophorbide photosensitizer for recurrent prostate cancer following definitive radiation therapy: assessment of safety and treatment response. J Urol. 2007; 178:1974–9. [PubMed: 17869307]

Trachtenberg J, Weersink RA, Davidson SR, Haider MA, Bogaards A, Gertner MR, Evans A, Scherz A, Savard J, Chin JL, Wilson BC, Elhilali M. Vascular-targeted photodynamic therapy (padoporfin, WST09) for recurrent prostate cancer after failure of external beam radiotherapy: a study of escalating light doses. BJU Int. 2008; 102:556–62. [PubMed: 18494829]

Verigos K, Stripp DC, Mick R, Zhu TC, Whittington R, Smith D, Dimofte A, Finlay J, Busch TM, Tochner ZA, Malkowicz S, Glatstein E, Hahn SM. Updated results of a phase I trial of motexafin lutetium-mediated interstitial photodynamic therapy in patients with locally recurrent prostate cancer. J Environ Pathol Toxicol Oncol. 2006; 25:373–88. [PubMed: 16566729]

Wang KK, Zhu TC. Reconstruction of in-vivo optical properties for human prostate using interstitial diffuse optical tomography. Opt Express. 2009; 7:11665–72. [PubMed: 19582081]

Weersink RA, Bogaards A, Gertner M, Davidson SR, Zhang K, Netchev G, Trachtenberg J, Wilson BC. Techniques for delivery and monitoring of TOOKAD (WST09)-mediated photodynamic therapy of the prostate: clinical experience and practicalities. J Photochem Photobiol B. 2005a; 79:211–22. [PubMed: 15896648]

Weersink RA, Forbes J, Bisland S, Trachtenberg J, Elhilali M, Brun PH, Wilson BC. Assessment of cutaneous photosensitivity of TOOKAD (WST09) in preclinical animal models and in patients. Photochem Photobiol. 2005b; 81:106–13. [PubMed: 15382963]

Whitehurst C, Pantelides ML, Moore JV, Brooman PJ, Blacklock NJ. In vivo laser light distribution in human prostatic carcinoma. J Urol. 1994; 151:1411–5. [PubMed: 8158797]

Zaak D, Sroka R, Stocker S, Bise K, Lein M, Hoppner M, Frimberger D, Schneede P, Reich O, Kriegmair M, Knuchel R, Baumgartner R, Hofstetter A. Photodynamic therapy of prostate cancer by means of 5-aminolevulinic acid-induced protoporphyrin IX - in vivo experiments on the dunning rat tumor model. Urol Int. 2004; 72:196–202. [PubMed: 15084761]

Zhu TC, Dimofte A, Finlay JC, Glatstein E, Hahn SM. Detector calibration factor for interstitial *in vivo* light dosimetry using isotropic detectors with scattering tip. Proc SPIE. 2005a; 5689:174–85.

Zhu TC, Dimofte A, Finlay JC, Stripp D, Busch T, Miles J, Whittington R, Malkowicz SB, Tochner Z, Glatstein E, Hahn SM. Optical properties of human prostate at 732 nm measured *in vivo* during Motexafin Lutetium mediated photodynamic therapy. Photochem Photobiol. 2005b; 81:96–105. [PubMed: 15535736]

Zhu TC, Finlay JC. Prostate PDT dosimetry. Photodiag photodyn ther. 2006; 3:234–46.

Zhu TC, Finlay JC, Hahn SM. Determination of the distribution of light, optical properties, drug concentration, and tissue oxygenation in-vivo in human prostate during motexafin lutetium-mediated photodynamic therapy. J Photochem Photobiol B. 2005c; 79:231–41. [PubMed: 15896650]

Zhu TC, Hahn SM, Kapatkin AS, Dimofte A, Rodriguez CE, Vulcan TG, Glatstein E, Hsi RA. In vivo optical properties of normal canine prostate at 732 nm using motexafin lutetium-mediated photodynamic therapy. Photochem Photobiol. 2003; 77:81–8. [PubMed: 12856887]

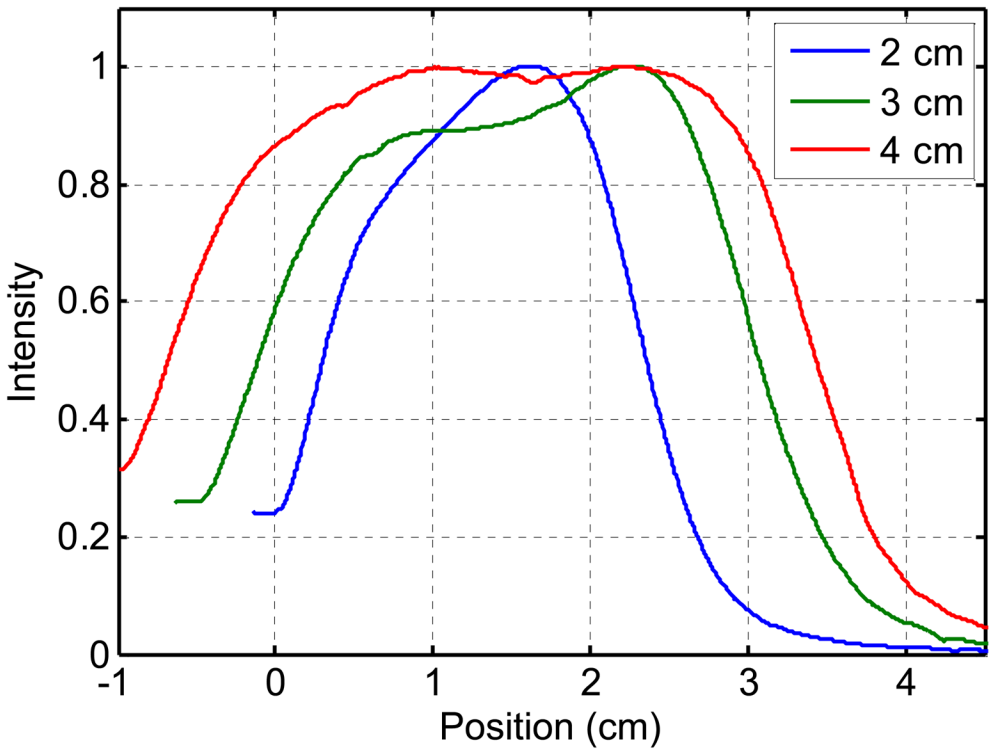

Figure 1.
Examples of the in-air light fluence rate distribution for 2, 3 and 4 cm long CDF placed 7mm from the isotropic detector. The intensity was normalized to be 1 at the maximum value

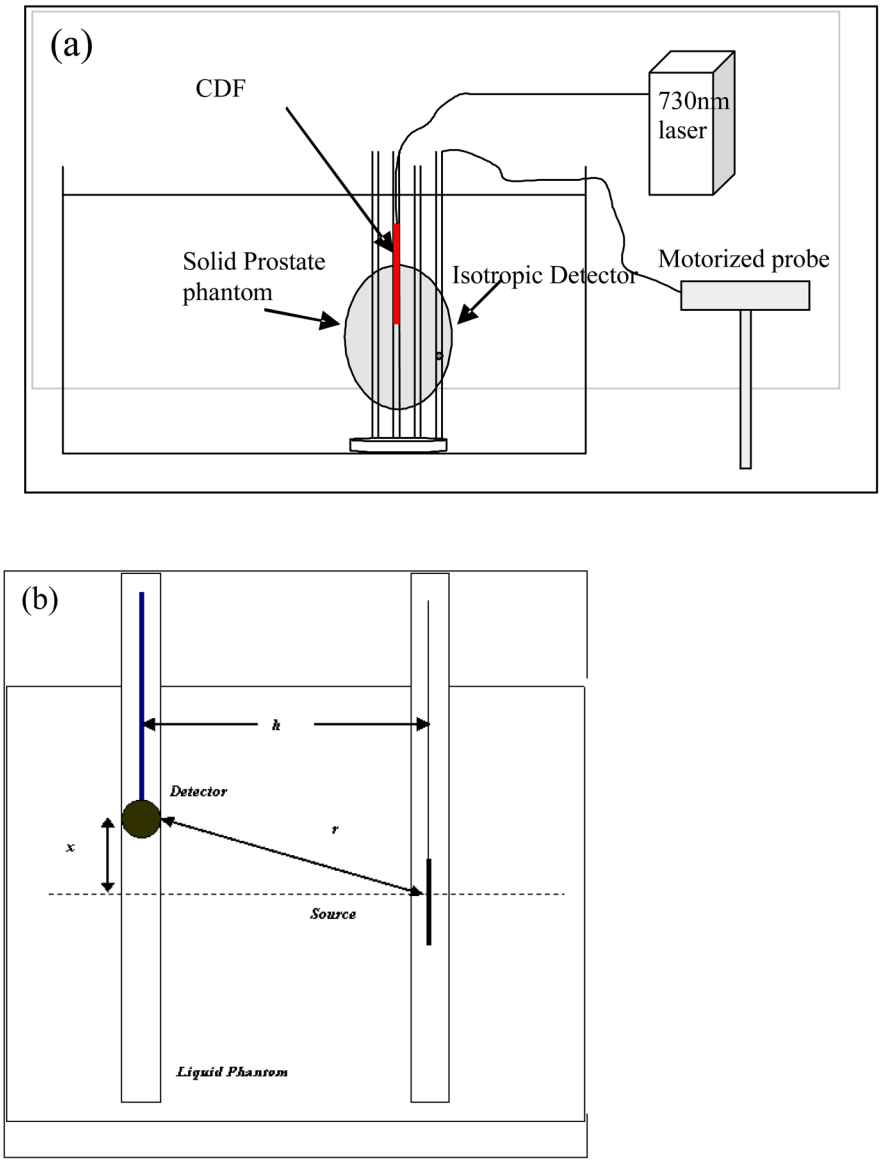

Figure 2.
Schematics for (a) the inhomogeneous prostate phantom and (b) the homogeneous liquid phantom. The distance between the CDF and the detector is *h*. The CDF is placed at a distance *x* from the surface of the phantom, while the detector is moved along the catheter.

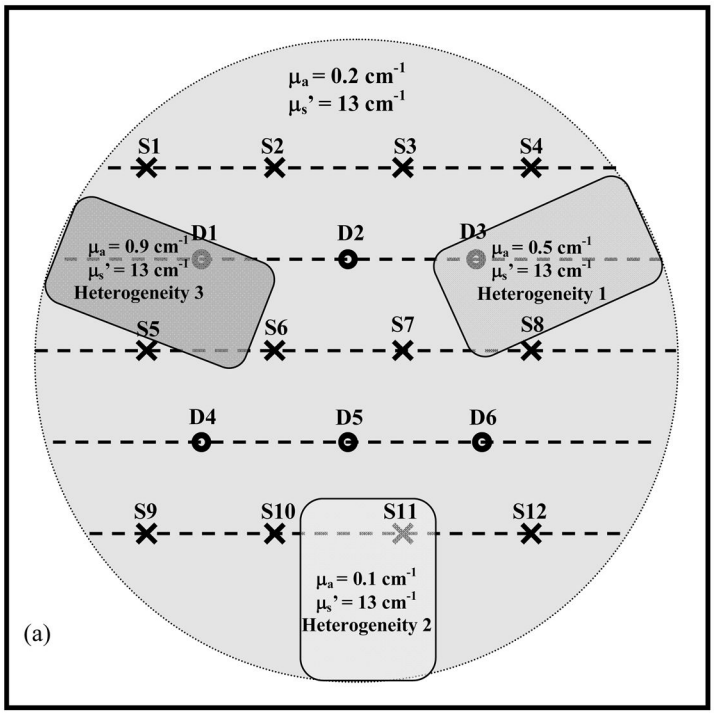

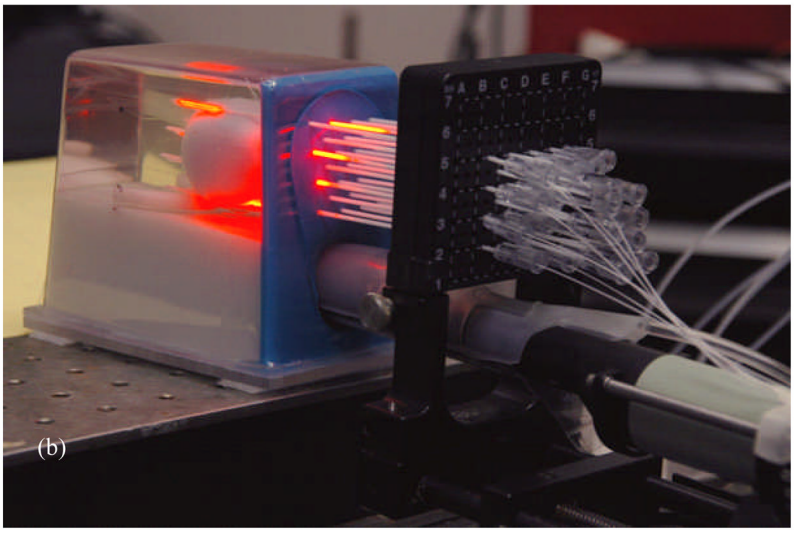

Figure 3.

(a) Diagram showing the needle positioning and the three in homogeneity placements throughout the prostate phantom. The CDF and detectors placement is shown by crosses and the dots, respectively. The three inhomogeneities are drawn as grey colored rectangles throughout the phantom. (b) Experimental setup for prostate measurement showing the phantom and the placement of the catheters inside the phantom.

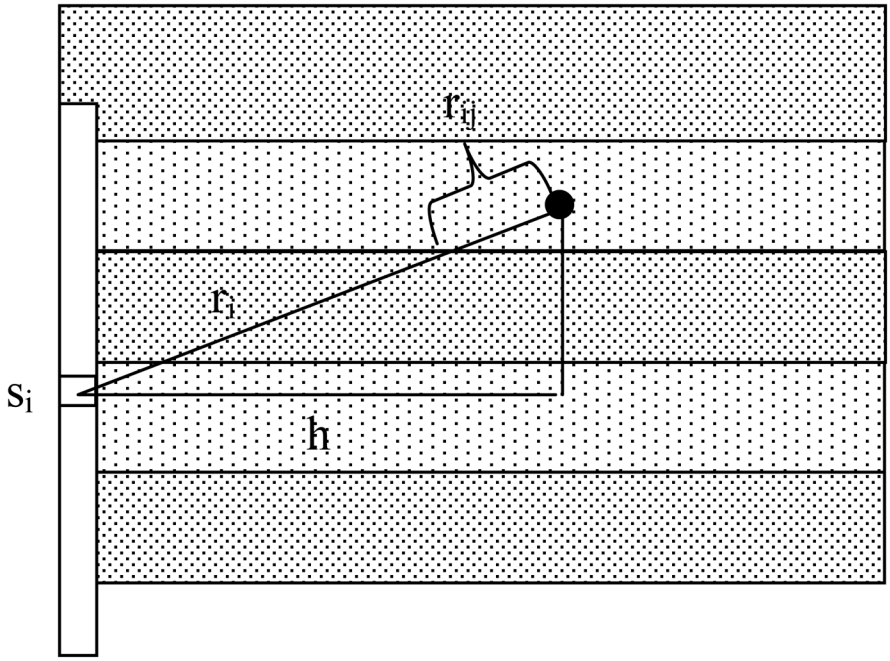

Figure 4.
Schematic of the linear diffuser model for a cylindrical diffusing fiber (CDF) with length composed of a series of point sources. The medium is divided into bins along the direction of the CDF's long axis, as shown. The optical properties used to calculate the contribution from source *i* to the point of interest (solid circle) are averaged along the line connecting the two, weighted by the fractional length contained in each bin (r_{ij}), as described in the text.

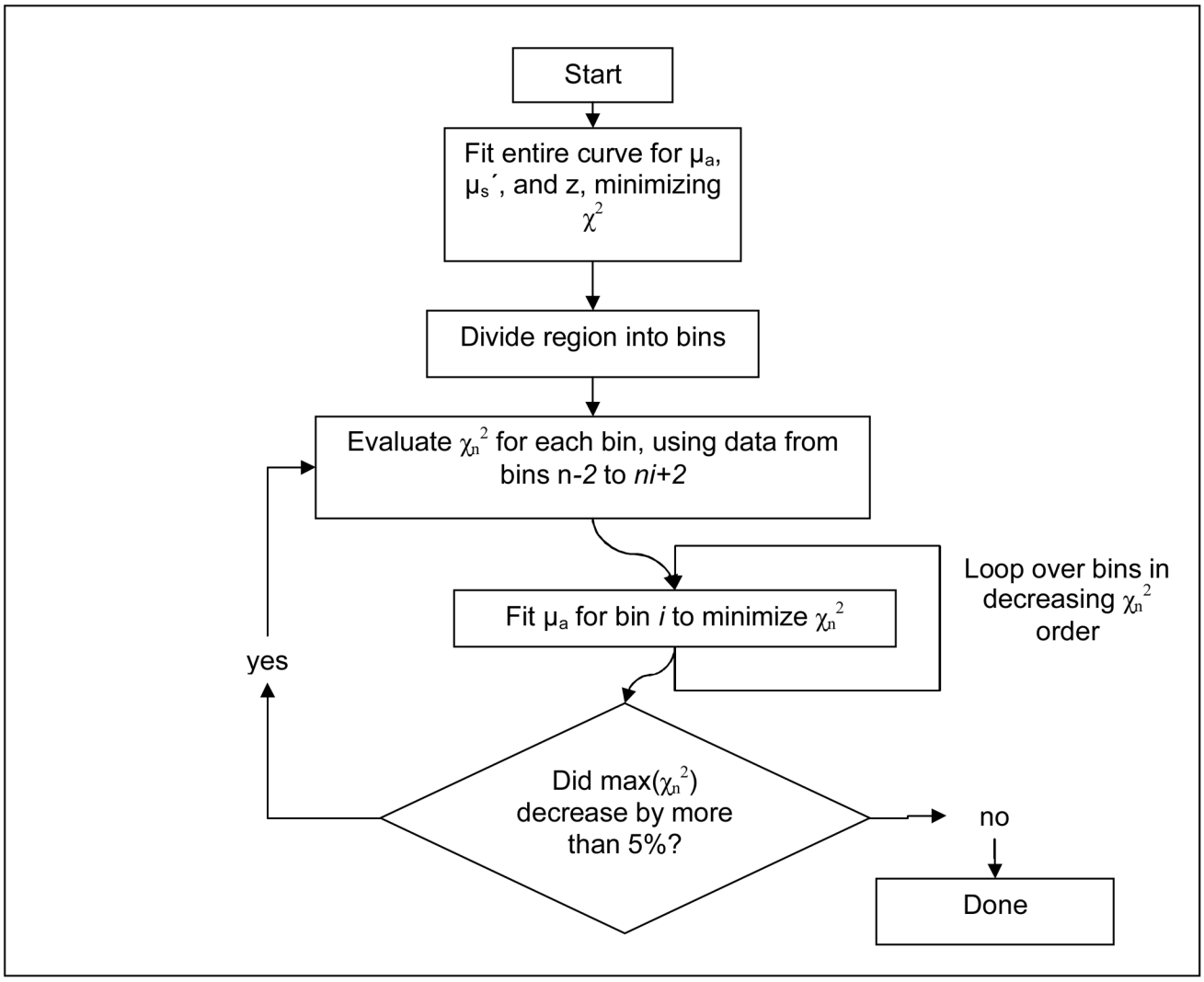

Figure 5.
Flowchart of the two-step fitting algorithm used to extract μ_a and μ_s' in heterogeneous media. The penalty functions χ^2 and χ_n^2 are calculated over the entire measured curve and the n^{th} bin and its two nearest neighbors, respectively.

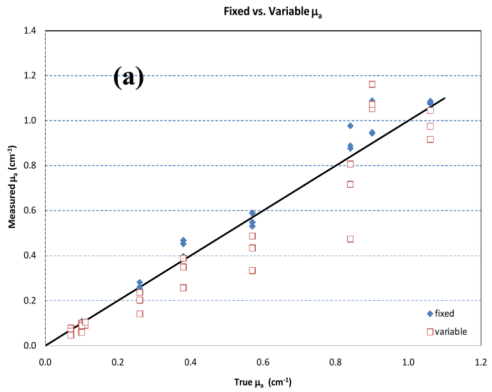

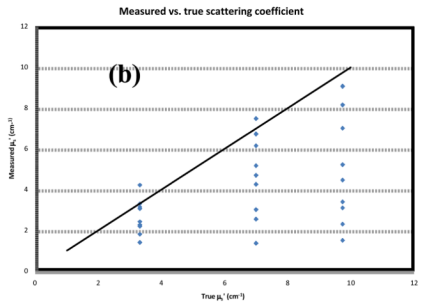

Figure 6.

(a) Absorption coefficient measured with fixed scattering coefficients vs. variable scattering coefficients for different CDF lengths. (b) Measured scattering coefficient vs. expected one for different lengths CDF. Data plotted for three reduced scattering coefficients: 3.3, 7 and 9.7 cm^{-1}.

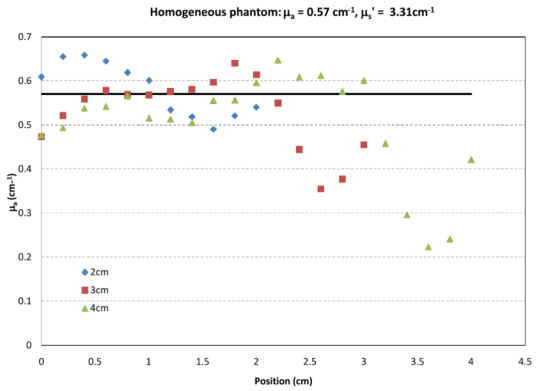

(a)

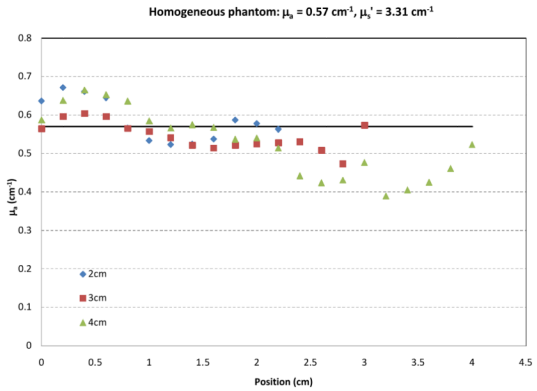

(b)

Figure 7.

Measured absorption coefficient μ_a vs. position along CDF using fixed *a priori* μ_s' for 2, 3 and 4 cm long CDFs using (a) in-air source profile and (b) uniform source profile. The solid line represents the expected value for μ_a (0.57 cm^{-1}). The expected value for μ_s' is 3.3 cm^{-1}.

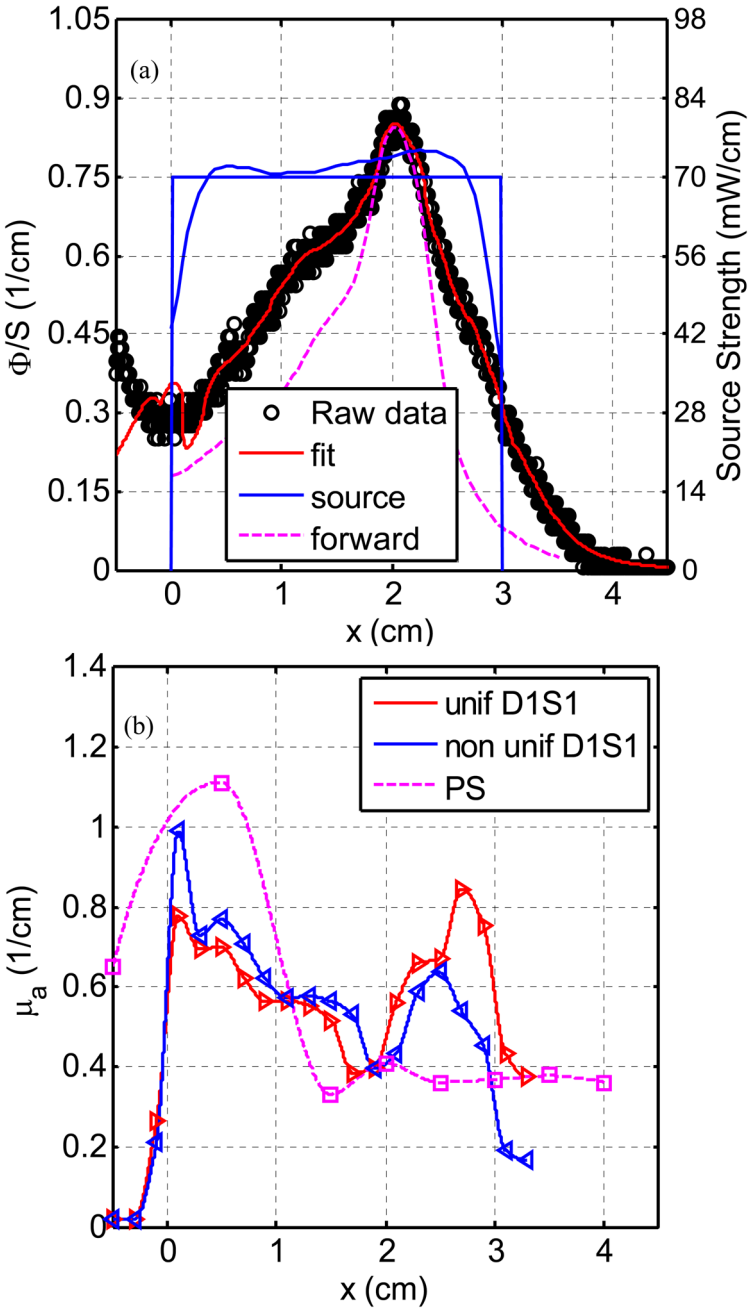

Figure 8 (a), (b)

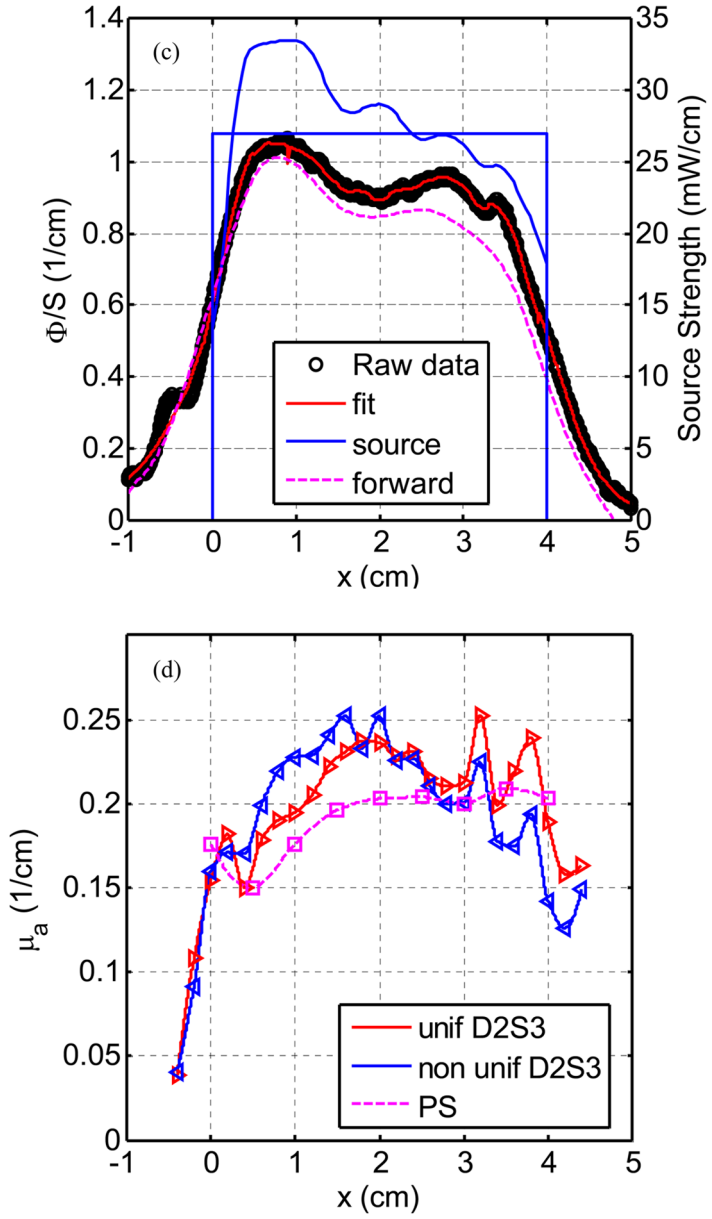

Figure 8 (c), (d)

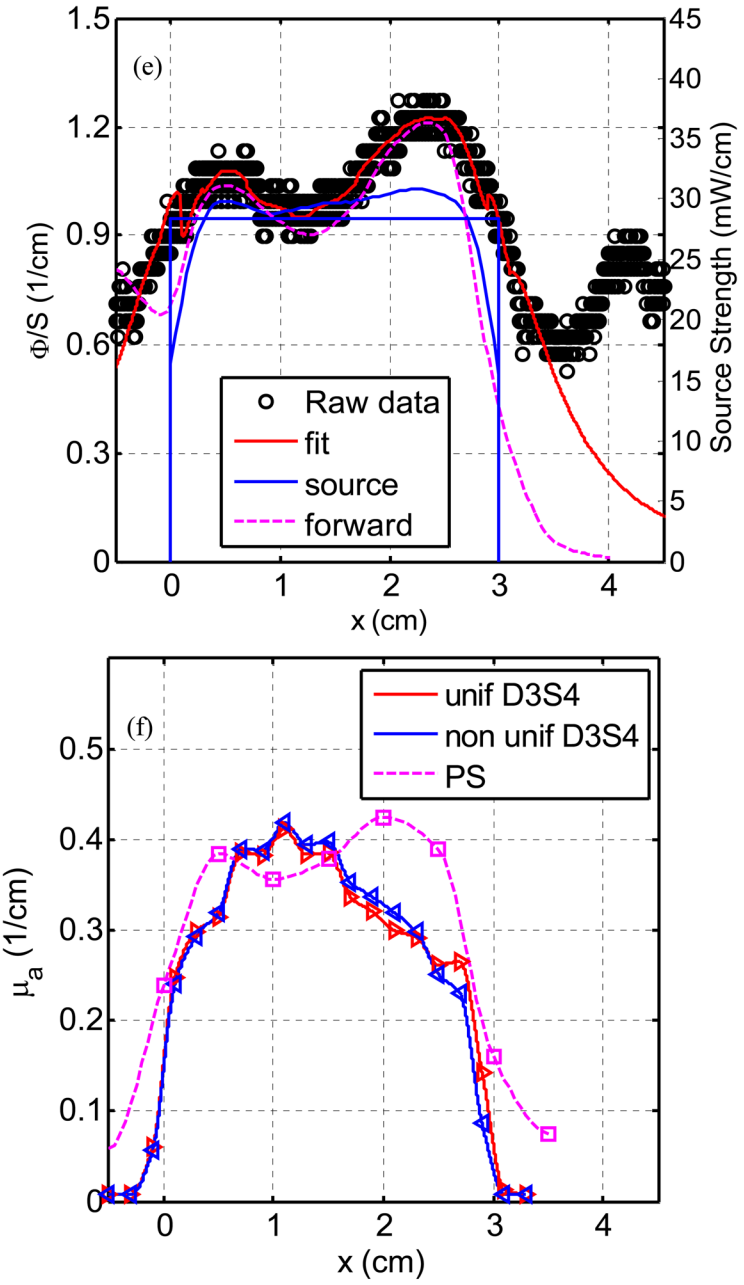

Figure 8 (e), (f)

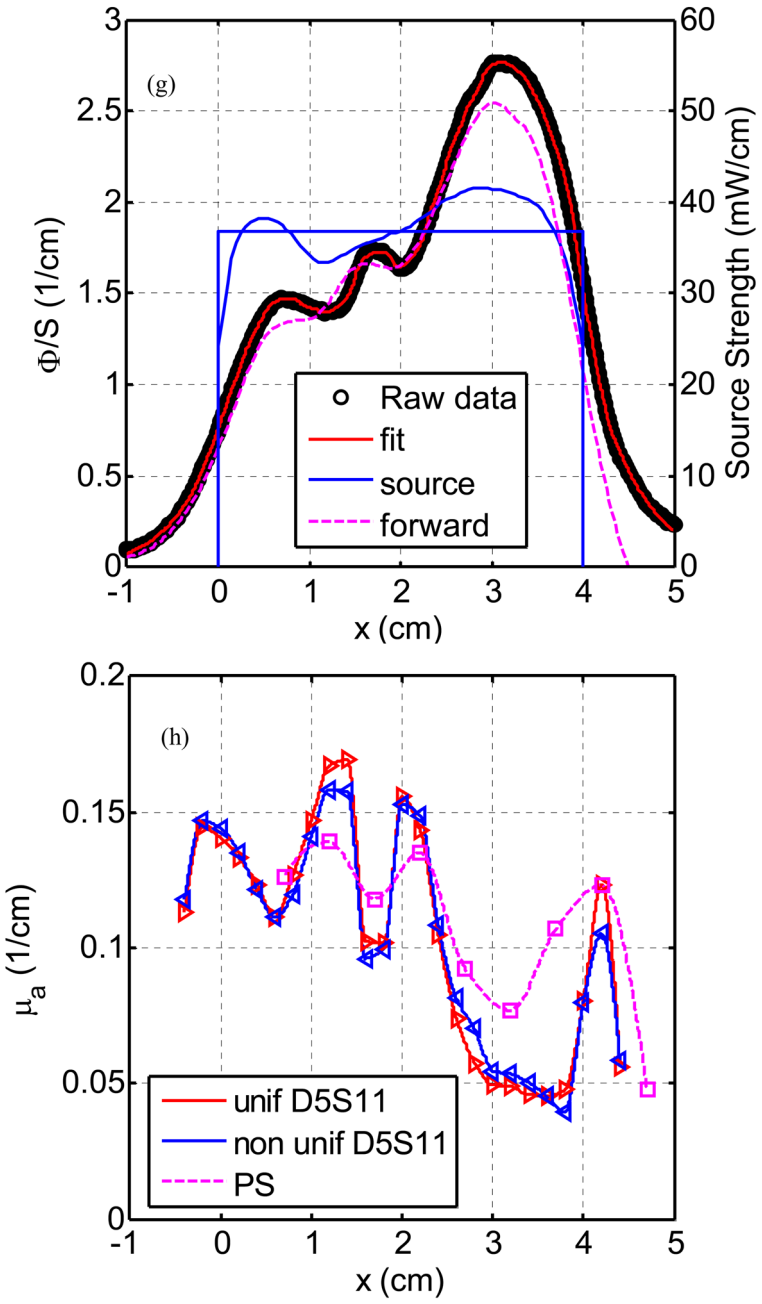

Figure 8 (g), (h)

Figure 8.

Light fluence rate (mW/cm^2) per source strength (mW/cm) (upper graph) and extrapolated absorption coefficients μ_a (lower graph) for various detector-CDF pairs in the heterogeneous prostate phantom. In the upper graphs, the dots represent measured data, the red line represents the fit, the solid blue lines represent the in air scan and the uniform source strength of that particular CDF, and the dashed lines represent the FEM-based forward calculation using the extrapolated optical properties, respectively, for (a) source 1 and detector 1, (c) source 3 and detector 2, (e) source 4 and detector 3, and (g) source 11 and detector 5. The light fluence rate per source strength and source strength use left and right vertical axes, respectively. In the lower graph, μ_a vs. position using point and CDFs are

plotted for (b) source 1 and detector 1, (d) source 3 and detector 2, (f) source 4 and detector 3, and (h) source 11 and detector 5.

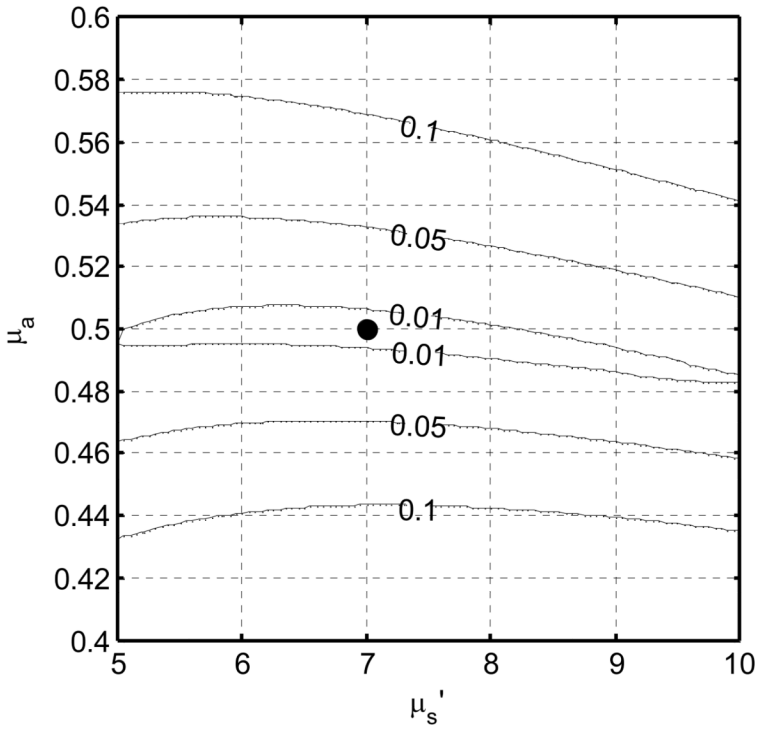

Figure 9.
RMS relative deviation in fluence rate measured along a line parallel to an ideal 4 cm source in an infinite medium. The simulated optical properties (where the deviation is zero) are indicated by the solid circle.

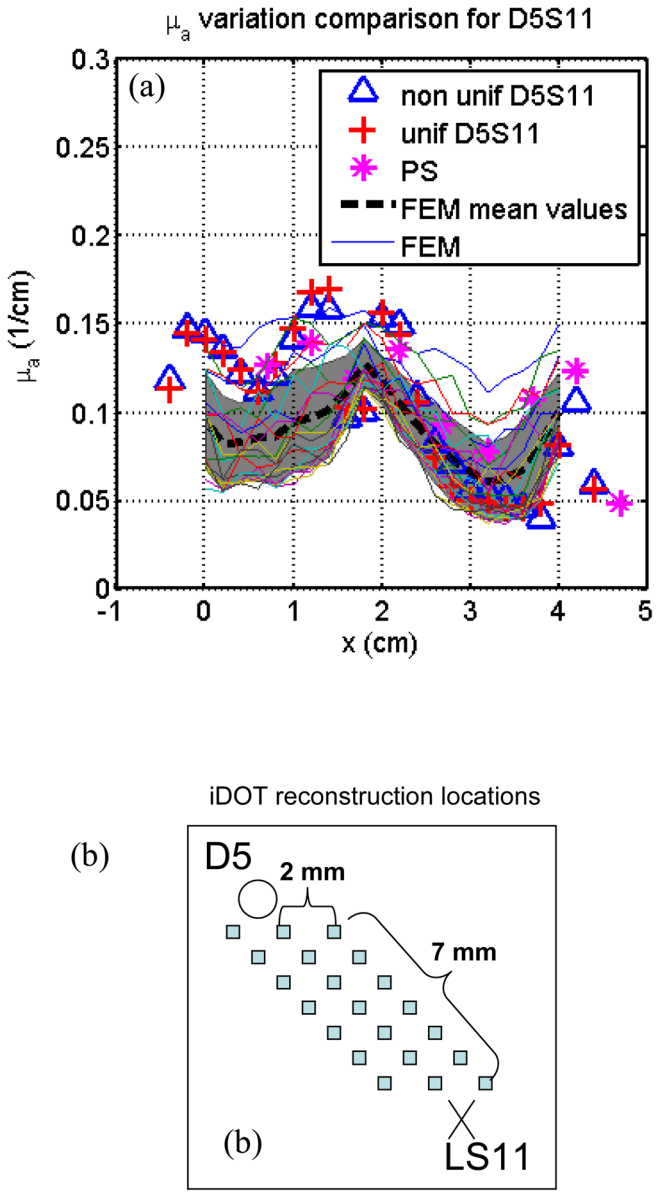

Figure 10.

Comparison with FEM reconstruction results from source 5 and detector 11. (a) FEM-reconstructed μ_a at different locations compared with the results by the fitting methods. Shadowing area represents mean μ_a values and their standard deviations along z direction. (b) The locations where the optical properties were reconstructed by FEM.

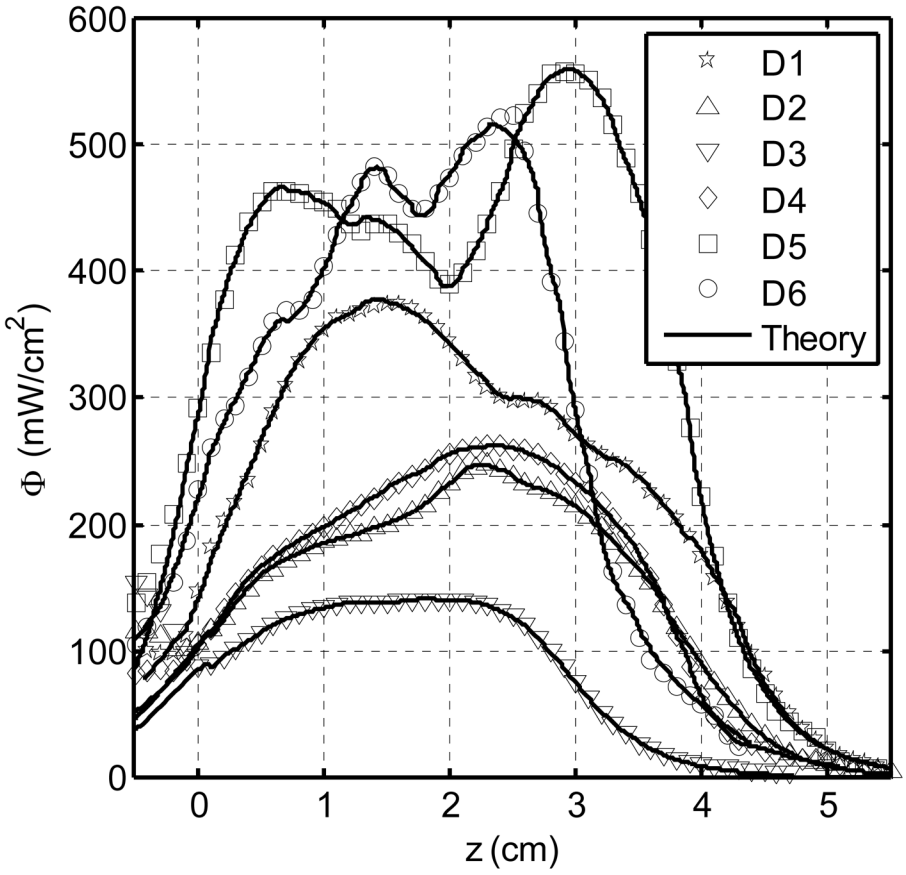

Figure 11.
Results of measured (symbols) and calculated (lines) light fluence rate at each detector locations (D1 – D6) according to Fig. 3 during PDT treatment. Each plot is the sum of the light fluence accumulated from the four adjacent channels. Each of the 12 CDFs has a uniform source strength of 100 mW/cm.

Table 1

A summary of accuracy of obtaining optical properties for CDF methods using fixed μ_s' (fixed fit), fixed μ_s' ± 20%, and extrapolated μ_s' (variable μ_s' fit). Lengths of CDF used were 2, 3 and 4cm. The first column specifies the length of CDF used. The second column specifies the optical properties of the phantom determined using a point source method. The third column specifies the mean and standard deviation (stdev) and the relative stdev (%) of the measured μ_a using fixed μ_s' to the known value. The difference (%diff) between measured mean value and the known value are also shown. The fourth column shows the mean μ_a value if the fixed μ_s' is off from the true values by ± 20% along with its difference to the true values (%diff). The fifth column specifies the measured mean and standard deviation (stdev) and the relative stdev (%) of the measured μ_a using variable μ_s' method. The difference between the measured mean value and the known values for μ_a and μ_s' are also shown. Optical phantoms were made with Liposyn concentrations varying from 0.3% to 1.52% and ink concentrations varying from 0.0023%, to 0.023%. The separation between the two catheters was 0.5 cm. The unit for μ_a and μ_s' is 1/cm.

CDF Length	Known values		Uniform Source Fixed-μ_s' fit				μ_s' +/− 20%		% diff		Uniform Source Variable-μ_s' fit					
	μ_a	μ_s'	μ_a								μ_a			μ_s'	μ_a	μ_s'
			mean	stdev	rel stdev	% diff	μ_a(+)	μ_a(−)	μ_a(+)	μ_a(−)	mean	stdev	rel stdev	mean	% diff	% diff
2cm	0.11	3.31	0.10	0.011	11%	−7%	0.13	0.06	26%	−39%	0.09	0.012	13%	3.15	−18%	−5%
	0.57	3.31	0.59	0.063	11%	3%	0.50	0.54	−16%	−8%	0.49	0.07	15%	2.43	−15%	−27%
	1.06	3.31	1.08	0.085	8%	2%	0.99	1.21	−8%	13%	0.98	0.10	10%	2.20	−8%	−33%
	0.07	6.99	0.07	0.016	23%	0%	0.10	0.04	37%	−46%	0.08	0.02	22%	7.48	11%	7%
	0.26	6.99	0.25	0.029	11%	−2%	0.28	0.24	10%	−6%	0.24	0.03	12%	6.15	−9%	−12%
	0.84	6.99	0.89	0.088	10%	6%	0.68	0.81	−24%	−9%	0.81	0.14	18%	2.55	−4%	−63%
	0.10	9.73	0.11	0.018	17%	6%	0.12	0.09	8%	−18%	0.10	0.02	17%	9.07	0%	−7%
	0.38	9.73	0.40	0.040	10%	4%	0.42	0.47	5%	17%	0.35	0.05	15%	5.23	−8%	−46%
	0.90	9.73	0.94	0.071	8%	5%	0.99	1.16	5%	22%	1.05	0.14	13%	3.40	17%	−65%
3cm	0.11	3.31	0.11	0.017	16%	−4%	0.14	0.08	30%	−25%	0.09	0.02	19%	3.07	−17%	−7%
	0.57	3.31	0.55	0.031	6%	−4%	0.57	0.48	4%	−13%	0.43	0.04	9%	2.27	−24%	−31%
	1.06	3.31	1.08	0.088	8%	2%	1.10	1.03	2%	−5%	0.92	0.11	12%	1.82	−13%	−45%
	0.07	6.99	0.07	0.018	26%	−3%	0.09	0.06	32%	−9%	0.06	0.02	27%	6.73	−9%	−4%
	0.26	6.99	0.26	0.045	17%	0%	0.26	0.19	0%	−27%	0.20	0.05	26%	4.70	−22%	−33%
	0.84	6.99	0.88	0.058	7%	4%	0.80	0.83	−9%	−6%	0.47	0.06	12%	4.26	−44%	−39%
	0.10	9.73	0.11	0.020	19%	7%	0.11	0.08	0%	−21%	0.09	0.02	23%	8.16	−10%	−16%
	0.38	9.73	0.45	0.022	5%	19%	0.48	0.48	6%	7%	0.39	0.04	10%	4.47	2%	−54%
	0.90	9.73	0.95	0.068	7%	5%	0.87	0.96	−8%	2%	1.07	0.13	12%	3.10	19%	−68%

CDF Length	Known values		Uniform Source Fixed-μ_s' fit				μ_s' +/− 20%		% diff		Uniform Source Variable-μ_s' fit					
	μ_a	μ_s'	μ_a								μ_a			μ_s'	μ_a	μ_s'
			mean	stdev	rel stdev	% diff	$\mu_a(+)$	$\mu_a(-)$	$\mu_a(+)$	$\mu_a(-)$	mean	stdev	rel stdev	mean	% diff	% diff
	0.11	3.31	0.10	0.046	45%	−6%	0.15	0.08	41%	−19%	0.10	0.05	46%	3.31	−5%	0%
	0.57	3.31	0.53	0.088	17%	−7%	0.52	0.52	−3%	−3%	0.33	0.12	37%	1.41	−41%	−57%
	1.06	3.31	1.09	0.290	27%	2%	1.00	0.93	−8%	−14%	1.05	0.21	20%	4.23	−1%	28%
	0.07	6.99	0.08	0.022	29%	10%	0.08	0.07	8%	−13%	0.05	0.02	43%	5.17	−33%	−26%
4cm	0.26	6.99	0.28	0.046	16%	8%	0.25	0.25	−11%	−11%	0.14	0.05	36%	3.02	−46%	−57%
	0.84	6.99	0.98	0.107	11%	16%	0.87	0.95	−11%	−3%	0.72	0.23	32%	1.37	−15%	−80%
	0.10	9.73	0.09	0.025	29%	−14%	0.10	0.07	12%	−20%	0.06	0.02	41%	7.01	−41%	−28%
	0.38	9.73	0.47	0.085	18%	23%	0.40	0.43	−14%	−8%	0.26	0.13	51%	2.31	−32%	−76%
	0.90	9.73	1.09	0.123	11%	21%	0.95	1.07	−13%	−2%	1.16	0.35	30%	1.51	29%	−84%

Table 2

A summary of accuracy in determining absorption coefficient using CDF methods with uniform source strength distribution (uniform fit) and actual source strength distribution (in-air scan fit) in liquid phantom. The first column specifies the length of CDF used. The second column specifies the absorption coefficient μ_a of the phantom determined using a point source method. The third column specifies the mean and the standard deviation (stdev) of the measured μ_a using the uniform profile. The percentage difference (%diff) between the mean and the known μ_a value is also listed. The fourth column specifies the mean and the stdev of the measured μ_a using in-air profile. Fixed known μ_s' was used in all fits. Lengths of CDFs used were 2, 3 and 4 cm. The three optical phantoms were made with Liposyn concentration of 0.71% (μ_s' = 3.31 cm^{-1}) and ink concentrations: 0.0023%, 0.011% and 0.023%. The unit of μ_a is 1/cm.

CDF Length	Known Values	Uniform Fit		In-air scan fit	
	μ_a	$\mu_a \pm \mu_a$	%diff (%)	$\mu_a \pm \mu_a$	%diff (%)
2cm	0.11	0.10 ± 0.01	−7%	0.11 ± 0.02	−5%
	0.57	0.59 ± 0.06	3%	0.59 ± 0.06	4%
	1.06	1.08 ± 0.09	2%	1.09 ± 0.10	3%
3cm	0.11	0.10 ± 0.02	−4%	0.11 ± 0.03	−1%
	0.57	0.55 ± 0.03	−4%	0.55 ± 0.06	−3%
	1.06	1.08 ± 0.09	2%	1.08 ± 0.08	2%
4cm	0.11	0.10 ± 0.05	−6%	0.10 ± 0.04	−7%
	0.57	0.53 ± 0.09	−7%	0.53 ± 0.08	−7%
	1.06	1.09 ± 0.29	2%	1.06 ± 0.18	0%

Phys Med Biol. Author manuscript; available in PMC 2012 November 07.

Table 3

Results for heterogeneous phantom. The first three columns list the known values and position of μ_a for the phantom background and three heterogeneities (numbered 1, 2, 3, clockwise starting from upper right corner) according to Fig. 3. Column four lists the mean and standard deviation of the measured μ_a for the background and the three heterogeneities. The last column specifies the percentage difference between the measured and the true μ_a value.

Description	Region specification	True μ_a values	Uniform Fit			In-air scan fit		
			Measured μ_a values	% diff	Max % diff	Measured μ_a values	% diff	Max % diff
Background	D2, S3 (Fig. 8d)	0.2	0.212±0.026	6%	26%	0.212±0.026	6%	26%
Heterogeneity 1	D3, S4 (Fig. 8f)	0.5	0.381±0.024	24%	33%	0.390±0.022	22%	30%
Heterogeneity 2	D5, S11 (Fig. 8h)	0.1	0.130±0.030	30%	69%	0.127±0.029	27%	57%
Heterogeneity 3	D1, S1 (Fig. 8b)	0.9	0.654±0.085	27%	37%	0.731±0.146	19%	37%